RSC Advances

ROYAL SOCIETY OF CHEMISTRY

www.rsc.org/advances

RSC Advances

ARTICLE

Graded-lattice AAO photonic crystal heterostructure for high Q refractive index sensing

Received 00th January 20xx,
Accepted 00th January 20xx

DOI: 10.1039/x0xx00000x

www.rsc.org/

Jungmin Lee,[a] Kyuyoung Bae,[a] Gumin Kang,[a] Minjung Choi,[a] Seunghwa Baek,[a] Do-sik Yoo,[b] Chang-Won Lee*[c] and Kyoungsik Kim*[a]

We present a low-cost and versatile optical sensor based on anodic aluminum oxide (AAO) graded-lattice photonic crystal heterostructure (PCH) template controlled by voltage pulse and electrolyte temperature. Designed PCH shows high Q factor up to ~ 55 from the first order side band peak in the reflectance spectra and vivid color change due to infiltrated analytes. Highly linear refractive index sensitivity "$d\lambda/dn$" up to 441 nm/RIU could be obtained independent of analytes' polarities. Superb perceptual colorimetric sensing performance was attained up to 0.01 according to CIELab tristimulus mapping analysis.

Introduction

Visually-recognizable noble-metal-free chemical sensor based on photonic bandgap (PBG) shift of one-dimensional (1D) photonic crystals (PCs) based on inorganic materials has been extensively studied owing to its scalable and low-cost fabrication process, excellent chemical and mechanical stability.[1] The PBG of the 1D PC in normal incidence case is given by Bragg formula:

$$m\lambda_{PBG}/2 = n_{1eff}d_1 + n_{2eff}d_2 \ , \qquad (1)$$

where m, λ_{PBG}, d_1, n_{1eff}, d_2, and n_{2eff} are the diffraction order, position of photonic bandgap, thickness and refractive indices of layer 1 and 2, respectively.[2] By analyzing Bragg formula, two distinct sensing schemes are possible by the photonic bandgap shift of 1D PC; the refractive index (RI) change and the volume change[3] of the target material.

For refractive index sensing, several porous 1D PCs have been proposed; GLAD deposition[4], dip-coating[5], self-assembly[6], and electrochemical etching[7-16]. Among various fabrication schemes, electrochemically etched porous silicon and anodic aluminum oxide (AAO) have been highlighted since they provide low cost, ease of fabrication, large surface area, range of accessible surface chemistries, and controllable optical and morphological properties such as nanopore size.[10, 15] Porous silicon has proven its novelty as a refractive index sensor[7, 9] leading to extensive studies for enhanced sensing performance. However, surface of the silicon should be passivated to obtain consistent signal with variation of environment over time.[17] More recently, to overcome passivation problems, AAO has been proposed as an alternative material.[18] AAO especially offers stable optical signals and mechanical robustness withstanding high pressures without surface passivation.

In the 1D PC system based on AAO, the photonic stop band is created by alternating AAO layers with different refractive index led by different porosities of each layer. The spectral position of optical interference effects depends on the periodic layer thickness of the photonic crystal, the porosity of AAO layers, and the refractive index of surrounding medium. According to the Bragg equation of porous inorganic 1D PCs, theoretical limit of PBG shift under infiltration of materials with specified refractive index (i.e. sensitivity) can be calculated by the porosities of each layer. Bragg equation for PBG peak with analyte of a porous 1D PC can be written as; [19]

$$\lambda_{PBG}/2 = \sqrt{p_1\varepsilon_{anal} + (1-p_1)\varepsilon_{Al2O3}}d_1 + \sqrt{p_2\varepsilon_{anal} + (1-p_2)\varepsilon_{Al2O3}}d_2 \ , \qquad (2)$$

where ε_{Al2O3}, ε_{anal}, p_1, and p_2 are the permittivity of alumina, the permittivity of infiltrated analyte, the porosity of layer 1, and the porosity of layer 2, respectively. With other variables fixed, PBG position is mainly dependent on the porosity of the 1D PC and the theoretical limit of the 1D PC refractive index sensor sensitivity depends on the resultant PBG shift. In general, more porosity enhances the refractive index sensitivity. The center location and the spectral linewidth of the PBG peak is decided both by periodicity of the PC and by the refractive index contrast between the adjacent high-index and low-index layers. In order to clearly detect PBG peak shift induced by analyte insertion, narrow original PBG peak

[a] School of Mechanical Engineering, Yonsei University, 50 Yonsei-ro, Seodaemun-gu, Seoul 120-749, Korea. E-mail: kks@yonsei.ac.kr
[b] School of Electronic and Electrical Engineering, Hongik University, 94 Wausan-Ro, Mapo-Gu, Seoul 121-791, Republic of Korea.
[c] Samsung Advanced Institute of Technology, Suwon, Korea. E-mail: cwlee42@gmail.com
* Corresponding authors
-JM Lee and KY Bae contributed equally to this work.

linewidth is advantageous. Recently, two notable approaches have been proposed to increase Q factor of the AAO. First, phase shifting microcavity introduces defect cavity between two PCs, so that creates the sharp transmission peak.[16] The reported peak has Q factor of ~ 24.2. Second approach is voltage compensation anodization method.[12] This requires precise voltage modulation in an anodization process to make AAO PC with highly aligned lattice. As a result, PBG peak of Q factor of ~ 27 was obtained.

In this work, by introducing "graded-lattice" profile, we demonstrate highly-sensitive refractive index sensor based on AAO graded-lattice photonic crystal heterostructure (PCH).[20] Here, we define the term "graded-lattice" as "gradually changing layer thicknesses". The demonstrated photonic structure breaks periodic symmetry to form a heterostructure[20] and shows high Q reflectance spectra of ~ 55 in the visible range. This heterostructure was fabricated by controlled pulsed cyclic anodization and subsequent wet chemical etching of AAO membrane to widen the nanopores and to connect the nearby channels. The entire AAO PCH has an enhanced porosity with a smooth refractive index profile, allowing large and distinguishable shift of the first-order side band reflectance peak under small refractive index change induced from inserted analyte. In addition, we test various polar and nonpolar analytes to confirm that our sensor does not rely on the polarity of analytes, which sometimes impedes the index sensing abilities.[8] As a result, refractive index sensitivity up to $d\lambda/dn$ ~ 441 nm/RIU has been achieved in this work, which is four-fold enhanced sensitivity compared to the previous report[12]. By controlling the temperature of the electrolyte during the anodization process, it was possible to choose the PBG and other side band positions of the AAO PCH allowing us to find the optimum spectral selectivity. We also take advantage of the large area uniform color of the AAO PCH, showing successful application to colorimetric sensing by mapping onto CIELab color space. The colorimetric analysis shows that our AAO graded-lattice PCH sensor provides perceptual color change corresponding to small refractive index changes down to ~ 0.01RIU.

Results and Discussion

Design and structural characterization of the graded-lattice PCH

With unique resonant spectrum near the heterostructure cavity, high Q factor can be obtained within the 2D photonic crystal slab.[21] We aimed to fabricate 1D PCH with gradually changing layer thicknesses profile, as shown in Fig. 1 (a). The upper part of the graded-lattice PCH has constant layer thickness periodicity; whereas the lower part has gradually changing layer thicknesses which will, in turn, induce effective graded-index profile. The constant-lattice PC is composed of 70 repetitive cycles of high and low density alumina layer with same cycle thicknesses and layer porosity. Each cycle has 240 nm lattice constant (6:4 for high and low density layer respectively) and the porosity of high and low density layer are set to 80% and 90%. The graded-lattice PCH, on the other hand, is composed of upper 15 cycles with having the same aforementioned structural properties of a constant-lattice PC and lower 55 cycles with continuously decreasing lattice constant down to 140 nm at the bottom end and fixed length ratio of 6:4 for high and low density layer. The corresponding effective refractive indices given by equation (2) are n_{1eff} = 1.165 for 80% porosity and n_{2eff} = 1.086 for 90% porosity.

For a quantitative comparison, reflectance spectra of PC with constant-lattice and the designed graded-lattice PCH were calculated by Finite-Difference Time-Domain (FDTD) method. FDTD simulation shows the reflectance spectra of the designed photonic band structure for the case of (black) constant-lattice PC and (red) graded-lattice PCH, respectively (Fig. 1(b)). A PC with 70 cycles of constant-lattice periodicity has the photonic bandgap peak with ~ 30 nm linewidth and Q ~ 18. Here, the linewidth was taken from full-width at half-maximum (FWHM) value of the peak after baseline subtraction provided by Origin 9.0 software. Therefore, it is not largely effective to extract enough sensitivity from the photonic bandgap peak shift induced from inserted analyte's refractive index. On the other hand, our newly-designed graded-lattice PCH breaks lattice periodicity and forms a unique index profile. The resultant photonic band structure has enhanced first order side band peak in the reflection spectrum (denoted as red curve), as shown in Fig. 1(b). The first order peak at higher side energy band of the modified PC has FWHM of about 8 nm with higher Q factor up to ~ 50, which allows more reliable peak shift tracking. Such a large reduction in the spectral linewidth stands for a meaningful improvement in the detection resolution limit or an improved overall Q factor when this graded-lattice PCH is employed in refractive index sensing.

Fig. 1(c) shows the mode profiles inside the designed graded-lattice PCH structure corresponding to (1) the highest peak of the PBG, (2) valley of between the PBG peak and the first order peak at higher side energy band, and (3) the first order higher side energy band peak, respectively. By breaking the periodicity, a resonant propagation modes emerges within the structure leading to optical fringes at side band.[22] The first order peak at higher side energy band could be clearly classified, assuring high sensitivity. Further description on FDTD simulations can be found on Additional Notes.

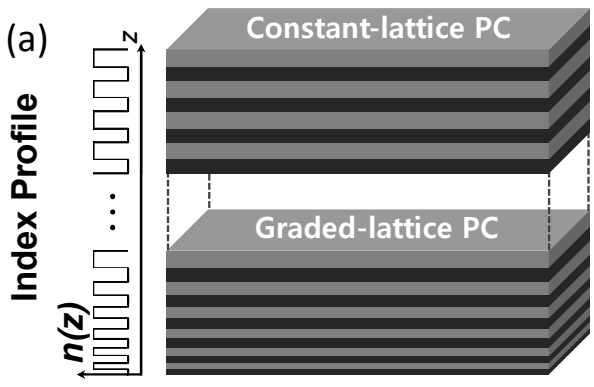

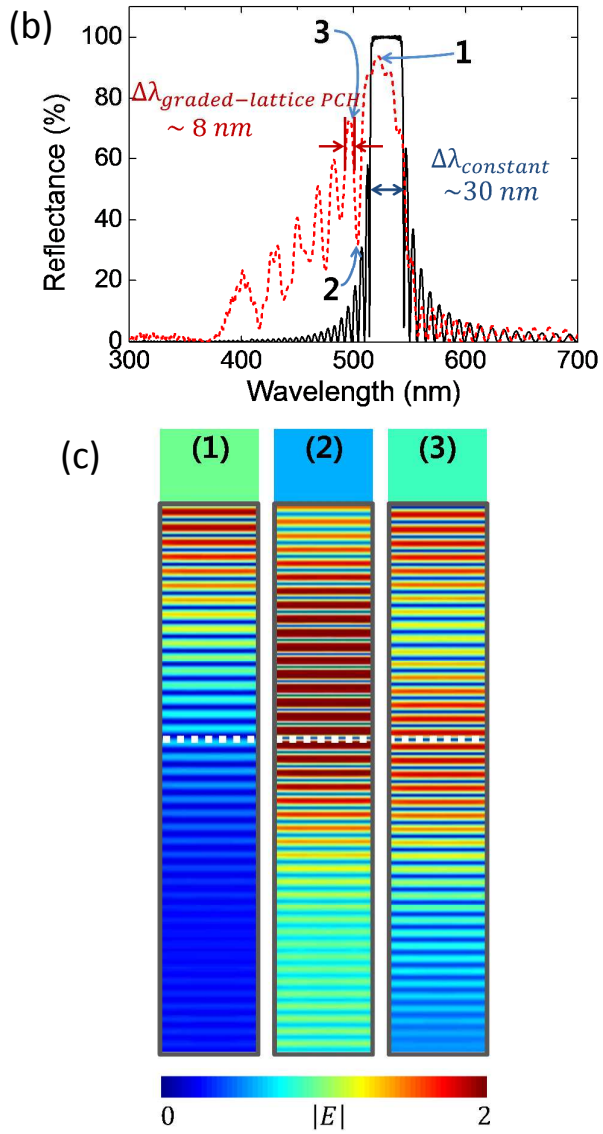

Fig. 1 Design of the graded-lattice PCH. (a) Schematic illustration of graded-lattice PCH. Upper part consists of 15 constant cycles with periodic index modulation, and lower part is composed of 55 graded-lattice cycles. The thicknesses of lower part cycles are designed to decrease linearly from 240nm to 140nm at the bottom and the thickness ratio between high and low density layer in each cycle is 6:4. With porosity of 80% and 90%, the effective refractive indices of high and low density layer are $n_{1eff} = 1.165$ and $n_{2eff} = 1.086$, respectively. (b) The comparison of simulated reflectance spectra from the PCs with perfectly periodicity (black) and with graded-lattice profile (red). The first order peak has ~ 8 nm FWHM while the PBG from periodic structure has ~ 30 nm FWHM. Due to the aperiodic index profile, the first order peak at higher side energy band of the PCH stands out with higher Q factor than the main PBG peak, which allows more sensitive index sensing. (c) The simulated mode profile of the selected peaks in (b). Gray boundary indicates the graded-lattice PCH structure designed in (a) and white dotted line represents the boundary between the constant-lattice and graded-lattice regions. The mode profile corresponding to peak (2) shows propagation mode arising from the strong resonance between two regions of different lattice constant profile of the graded-lattice PCH.

Preparation of the AAO graded-lattice PCH

Uniform, chemically stable, and highly porous photonic crystal heterostructures made of AAO can be fabricated by well-developed anodization technique of aluminum.[23] As-received aluminum disk (99.999%, Good fellow) is used as the substrate material. After annealing at 500°C for 5h, the Al disk was electropolished in a mixture of perchloric acid ($HClO_4$) and ethyl alcohol (C_2H_5OH) (volume ratio 1:10) by a constant voltage of 20 V for 10 min to achieve mirror-finished surface. The graded-lattice profile can be obtained by changing effective lattice constant induced by pulsed cyclic anodization and controlling of electrolyte stirring condition.[23-25] In the anodization process, mass transport of anionic species through nanochannals is closely related to the growth rate of AAO. Diffusion of anionic species decreases with longer nanochannel, as a result, the effective lattice constant of AAO PCH decreases.

The entire fabrication procedure consists of three steps. The first anodization was carried out at a constant voltage of 52 V in 0.3M oxalic acid at 15°C for 15 h. The formed alumina layer was then removed by chemical etching in a mixture of phosphoric acid (6wt%) and chromic acid (1.8wt%) at 80°C for 5 h. Subsequently, the second anodization was performed on the groovy Al surface using same conditions as the first anodization process except for the applied voltage.[26]

To obtain the graded-lattice PCH structure, a periodically modulated voltage is applied during the second anodization process.[27] Each cycle consists of three sections; (i) a constant voltage at V_H for 30 s, (ii) a sinusoidal decaying ramp from V_H = 53 V to V_L = 30 V for 90 s, and (iii) a continuous voltage value of V_L lasting for 2 min. Anodization voltage curve and following current density profile is presented in Fig. 2(a). The tendency of current density relative to anodizing voltage is closely related to the barrier layer thickness at the pore bottom.[23] This alumina layer works as a potential barrier for electric field between electrolyte and aluminum substrate. In Fig. 2(a), sharp current flow at the beginning of region (i) originated from the thin barrier layer of region (iii), which is adequate for V_L but low potential barrier for V_H. Similarly, steep decrease of current density at the region (ii) originated from the thick barrier layer formed by V_H of region (i). As the barrier layer thickness adjusts the applying voltage, current density recovered at the end of the region (i) and (iii). For 70 cycles of anodization, surrounding conditions were carefully maintained to exclude any change of environmental effects.

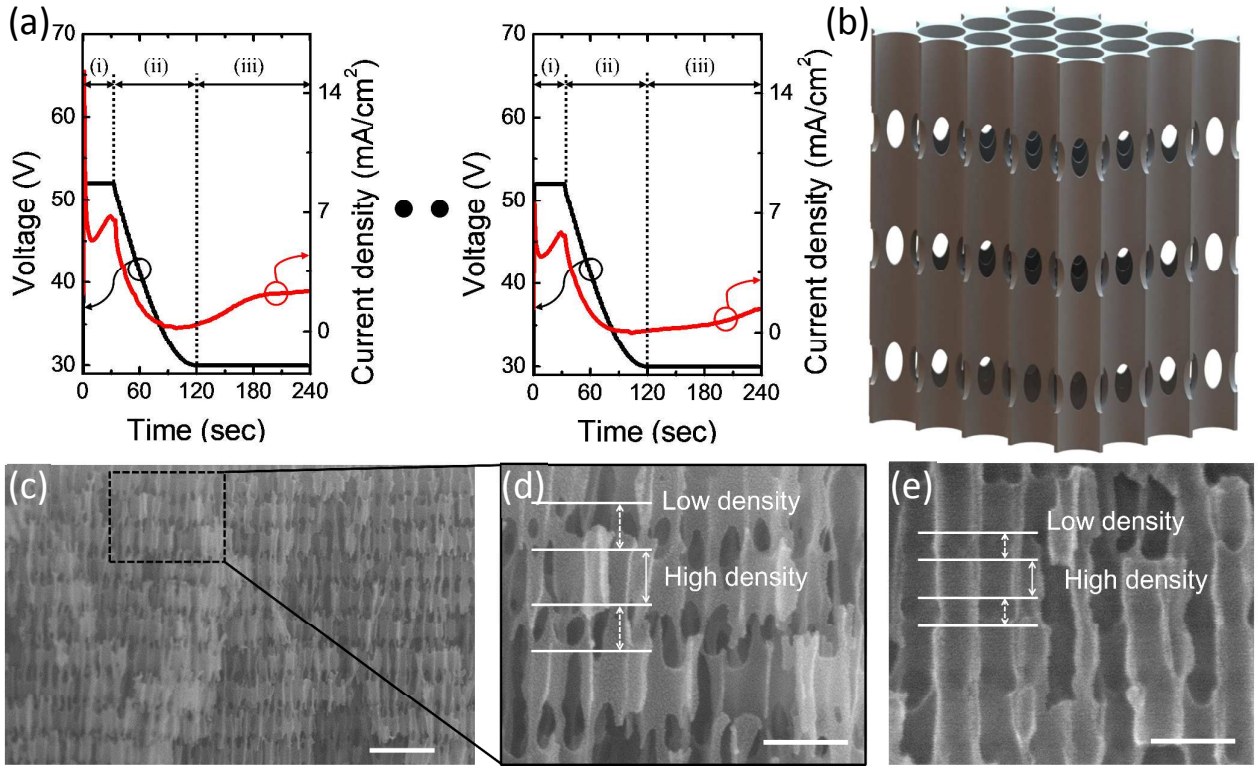

Fig. 2 (a) Temporal current density trace (red) with respect to the applied voltage (black) during the second anodization process for the upper layers (left) and lower layers (right). Under the same applied voltage trace, anodization current density decreases for the lower layers because diffusion or transport of the anionic species is reduced due to increased nanopores network length. (b) Schematic structure of the AAO graded-lattice PCH showing how the 3D AAO networks and nanopores are formed. (c), (d) and (e) Cross sectional SEM images of the AAO graded-lattice PCH fabricated by periodic anodization at 15°C and the subsequent pore widening process with phosphoric acid (6wt%) at 30°C, for 53 min. White scale bars correspond to 500 nm for (c) and 200 nm for (d) and (e). (c) and (d) show upper part of the AAO graded-lattice PCH and (e) shows lower part. Upper part has low density of nanopores and relatively longer lattice periodicity. Lower part, on the other hand, has more porosity with dented structures resulting in shorter lattice periodicities.

The electrolyte flow is controlled with electrical stirrer to make the speed of 10 cm/s parallel to the Al surface. In the early stage of anodization, this electrolyte flow induces forced convection condition to make uniform anodization rate of AAO pores, which made the constant-lattice photonic crystals.

After about 15 cycles of uniform anodization (depth ~ 3.5 μm), increased pore length disturbed the circulation of electrolyte from AAO surface to bottom and gradually decreased the flow rate of oxygen-containing anionic species.[23] Consequently, the overall current density became smaller cycle by cycle (Fig. 2(a)), which resulted in graded-lattice profile below the upper photonic crystal. After the second anodization process, Al substrate at the center of the Al disk was etched by a saturated solution of copper chloride (IV) ($CuCl_4$) solution in water and hydrochloric acid (HCl) to obtain free-standing AAO graded-lattice PCH membrane. At the second anodization process, we prepared samples under three different electrolyte temperature conditions; 14.5°C, 15°C, and 15.5°C. The elevated electrolyte temperature leads to higher current density resulting in thicker profile of overall AAO PCH.[13, 23] In this way, the gradient of the graded-lattice photonic crystal could also be tuned.

Lastly, pore-widening step was performed by wet-chemical etching in phosphoric acid (6wt%) at 30°C for 50 min so that the inner structure of AAO graded-lattice PCH reaches maximum porosity, while maintaining mechanical robustness. After 53 min of pore widening process, we observed that the AAO structure loses its structural stability. It is important to increase the porosity of the AAO PCH by optimized chemical etching with keeping structural stability. In the sensing application, the analyte should fill the AAO PCH entirely to minimize the volume of the remaining air. Our fabrication scheme, based on controlled etching condition, is very effective for this purpose. The fabricated transversal nanochannels, which interconnect adjacent longitudinal nanopores at some periodic points, form a 3D nanochannel network allowing efficient analyte infiltration, as illustrated in Fig. 2(b).[25] As a result, the porous layer replaced by the absorbed analyte provides reproducible peak shift in the reflectance spectra and enough sensitivity for refractive index change of the analyte.

Figure 2(c) shows the representative cross sectional scanning electron microscope (SEM) image of a fractured profile of the AAO PCH fabricated by 70 cycles of periodic anodization at 15°C and the pore etching process with optimized conditions. The overall AAO PCH structures show repetitive profile with high density and low density layers. Upper part consists of vertical pores with interconnecting nanochannels along the horizontal directions of the image and the lattice constant, which includes the thickness of low density layer and high density layer, is about ~ 235 nm (15 cycles, Fig. 2(d)). Lower parts present a slightly different pore profiles with

dented low density layers and the reduced lattice constant of ~ 150 nm at the lower end of the AAO PCH (55 cycles, Fig. 2(e)). In addition, measured upper and lower structures showed good accordance with the design in Fig. 1(a).

Spectroscopic characterization and Refractive index sensing ability

To investigate the spectral properties of the AAO graded-lattice PCH system, we measured the reflectance spectra and took pictures under normal incident white light source, as shown in Fig. 3. Detailed methodology of reflection spectroscopy can be found from our previous reports[1, 28, 29]. The center of the as-prepared AAO PCH sample fabricated at 15°C electrolyte temperature shows uniform and vivid sky blue color, as shown in the inset of Fig. 3(a). The outer opaque white color is due to the scattered light from unetched aluminum. The measured reflection spectra of the free-standing AAO graded-lattice PCH in air shows good agreement with the simulated FDTD result shown in Fig. 1(b). Due to the graded-lattice profile, several high Q peaks emerge in the higher side energy band. The first order peak at 479 nm shows about $\Delta\lambda_{1st\ mode}$~ 8.6 nm spectral FWHM with Q factor of ~ 55, which is 2.6 times larger than that (Q ~ 22) of the zeroth mode peak centered at 520 nm with FWHM of $\Delta\lambda_{0th\ mode}$ ~ 24 nm. This Q factor is also three times larger than the PBG peak of the perfectly periodic PC and almost twice larger than the previously reported results.[12, 16] In order to quantify the refractive index sensing capability, we measured the reflectance spectra of the AAO PCH with a series of polar and nonpolar analytes immersed at ambient condition, as shown in Fig. 3(b). Tested analytes are water (polar, n=1.3323, blue), anhydrous ethanol (polar, n=1.3606, sky blue), anhydrous n-hexane (nonpolar, n=1.3719, green), isopropyl alcohol (polar, n=1.3742, orange), cyclohexane (nonpolar, n=1.4225, red), and trichloroethylene (nonpolar, n=1.4777, violet). The measured reflectance spectra are arranged from lowest (bottom) to highest index (top) to clearly show spectral shift to longer wavelength with increasing refractive index of the immersed analyte. Particularly, the peak shift of the first order side band shows high degree of linear relationship with the index showing sensitivity up to $d\lambda/dn$ ~ 385 nm/RIU and regression coefficient R^2 of 0.99857. This sensitivity is more than 3.5 times higher than previously reported index sensitivities[12]. We note that our refractive index sensor produces good linearity regardless of the polarity of analyte. Based on previous study,[8] polarity of the infiltrated analytes may affect the sensitivity of AAO PC which makes overall refractive index sensing ability obscure. It is mainly due to inner vacancy formation between non-polar analytes and alumina surface. Regarding this issue, we especially included test analytes with very close refractive indices; anhydrous n-hexane (nonpolar, n=1.3719) and isopropyl alcohol (polar, n=1.3742) to find out the effect of the polarity, however no significant effect was observed. As it can be seen in Fig. 3(b), the green line and orange line, which represent nonpolar anhydrous n-hexane and polar isopropyl alcohol respectively, fit perfectly into the linear guideline. We speculate the 3D interconnected nanochannels effectively average out the polarity of the analytes in our sensor by successfully excluding the possibilities of air bubbles.

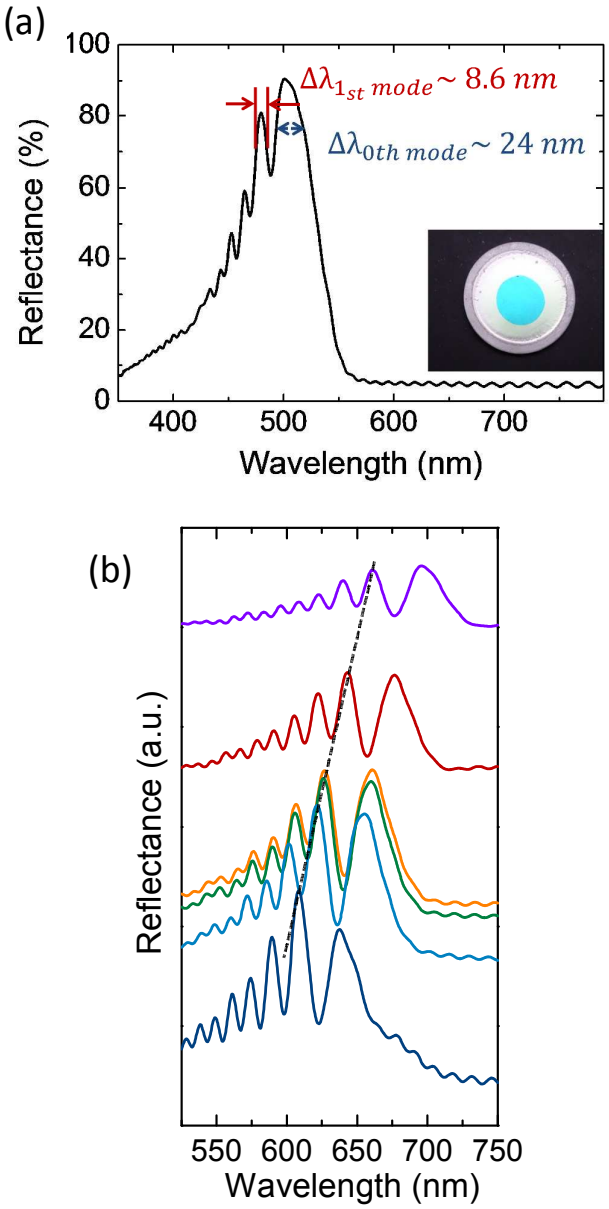

Fig. 3 Reflection spectrum and refractive sensing ability of AAO graded-lattice PCH. (a) Measured reflection spectra of the free-standing AAO PCH in air, which shows good agreement with FDTD computed results. Due to the graded-lattice profile, bulk PBG splits into several high Q peaks and the 1_{st}mode peak shows about ~ 8.6 nm FWHM. Inset is a color photograph of AAO PCH in air. (b) The reflectance spectra show peak shifts to longer wavelengths with immersion of water (polar, n=1.3323, blue), anhydrous ethanol (polar, n=1.3606, sky blue), anhydrous n-hexane (nonpolar, n=1.3719, green), isopropyl alcohol (polar, n=1.3742, orange), cyclohexane (nonpolar, n=1.4225, red), and trichloroethylene (nonpolar, n=1.4777, violet), respectively. The refractive index sensitivity, which is obtained by the linear regression of the peak shift of the first order side band, reaches up to $d\lambda/dn$ ~ 385 nm/RIU for this AAO PCH fabricated at 15°C electrolyte temperature.

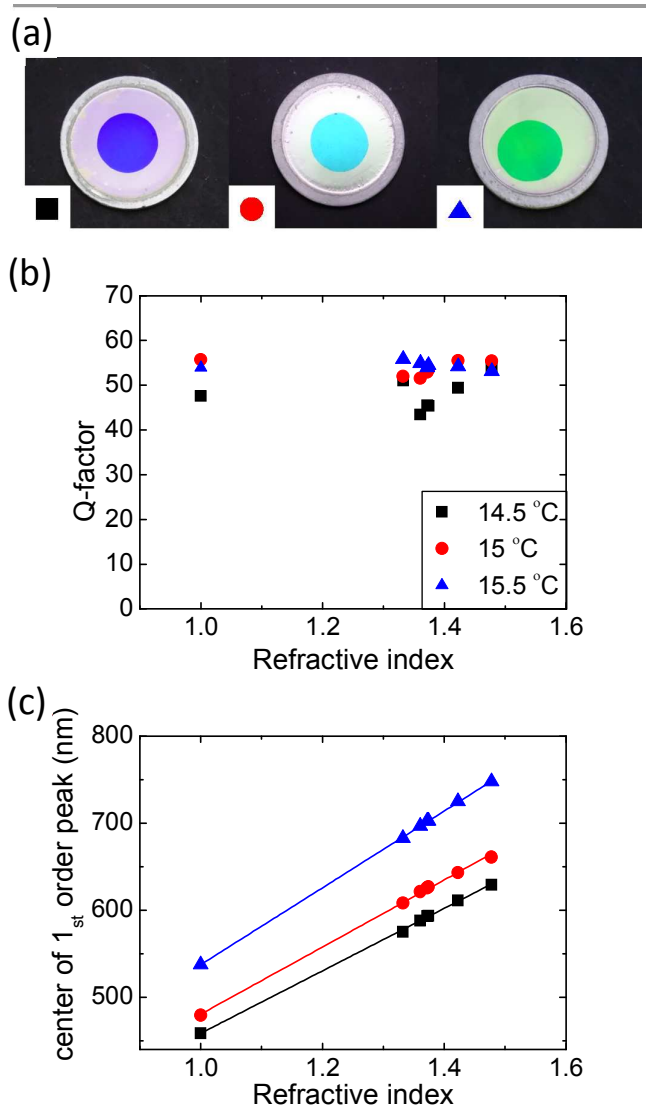

Fig. 4 (a) Optical photograph of the as-prepared AAO PCHs in air, anodized at electrolyte temperatures of 14.5°C (left), 15°C (center), and 15.5°C (right). (b) Q-factors of the first order higher side energy band peak with the increasing refractive index of analytes. Square, circle, and triangle symbols indicate the samples anodized at 14.5°C (black square), 15°C (red circle) and 15.5°C (blue triangle), respectively. (c) Center wavelength of the first order peak of AAO PCH sensors anodized at three different temperatures infiltrated with six different analytes. With increasing electrolyte temperatures, overall reflectance spectrum moves to longer wavelength. The observed peak location has good linear relationship with the refractive indices of the analytes, showing large sensitivities of $d\lambda/dn$ ~ 359 nm/RIU (14.5°C), ~ 385 nm/RIU (15°C), ~ 441 nm/RIU (15.5°C) respectively.

Even higher sensitivity can be obtained with samples anodized at elevated electrolyte temperature. Figure 4(a) shows the color images of the AAO graded-lattice PCHs fabricated at 14.5°C, 15°C, and 15.5°C, respectively. The color of the prepared 1D AAO photonic crystal is caused by the all the interference peaks and the photonic band gap in the reflectance spectra. Compared to the PCH fabricated at 15°C, other two PCHs show a bit of color nonuniformities. The effect of the elevated electrolyte temperature during the anodization process is the layer thickness increase of the AAO PCH.[30] As a result, the overall reflectance spectra move to longer wavelength region. Interestingly, the Q-factors of the first order side band peak show more than 40 in all cases. We plot the Q-factors after infiltration of various analytes, as shown in Fig. 4(b). The Q-factors of the AAO PCH at 14.5°C electrolyte temperature show generally low values whereas those of the PCHs at 15°C, and 15.5°C electrolyte temperatures are high enough for refractive index sensing. As a result, the refractive index sensitivities of the 15.5°C PCH sample reaches up to $d\lambda/dn$ ~ 441 nm/RIU, as shown in Fig. 4(c). The 14.5°C and 15°C samples show $d\lambda/dn$ ~ 359 nm/RIU and ~ 385 nm/RIU, respectively. The result shows the similar tendency of refractive index sensitivities with the initial first order side band peak position of as-prepared samples; 458 nm for 14.5°C, 480 nm for 15°C and 537 nm for 15.5°C. Based on following observations, we assume that our fabrication scheme could provide the spectral selectivity with sufficient degree of uniformity through anodization temperature, while maintaining several conditions such as anodization voltage, stirring intensity and etching rate, which are hard to customize for each sample.

Colorimetric sensing; CIELab color space

The color of the prepared AAO PCH is affected by all the interference peaks and the photonic stop band. Since photonic band depends on the lattice structure (including periodicity) and material's dielectric permittivity and magnetic permeability, the color can be changed with respect to the viewing angle as well as the analyte infiltration.[31] To show objective colorimetric sensing ability, a standard color identification scheme is necessary. In this study, refractive index change is perceptually recognized by color gamut analysis.

To evaluate colorimetric sensing performance, we map the image data to the CIELab 1931 tristimulus color space as the basis of colorimetric sensing. The CIELab color space is one of the most widely used color spaces for device-independent color representation.[4] In CIELab color space, all colors are represented by the tristimulus values, lightness L^* and chromaticities a^* and b^*. The total quantitative difference ΔE between the two colors is given by the following formula:

$$\Delta E = \sqrt{\Delta L^{*2} + \Delta a^{*2} + \Delta b^{*2}}, \qquad (3)$$

where ΔL^*, Δa^*, Δb^* are the differences between two arbitrary points in lightness L^* and chromaticities a^* and b^* axes. ΔE, which means Euclidean distance between the two color points, represents the perceived color difference by the observer. It should be noted that a range of auxiliary factors such as surrounding background radiation, illumination conditions, and observer perception may affect the colorimetric sensitivity. However, it is widely accepted that the approximate minimal threshold of perceptual color change is given by $\Delta E = 1$.[32]

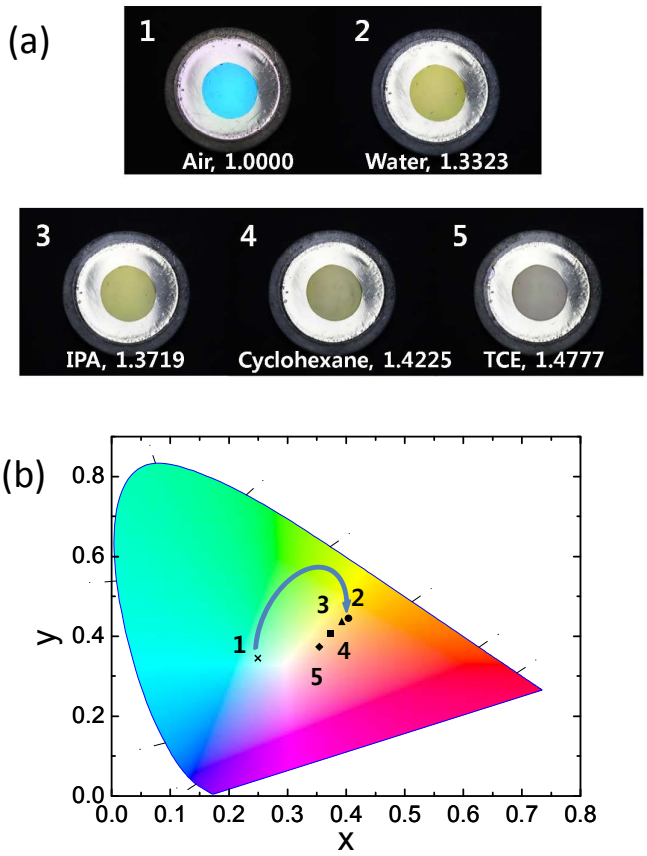

Fig. 5 (a) Color photographs of the 15°C AAO graded-lattice PCH taken with absorbing series of analytes from air to TCE. (b) CIE 1931 chromaticity diagram of the color response of AAO PCH calculated from Table 1 with 1 (air, **x**), 2 (water, ●), 3 (isopropyl alcohol, ▲), 4 (cyclohexane, ■) and 5 (trichloroethylene, ◆). The arrow indicates the color change trends between the point 1 and 2.

Figure 5(a) shows color photographs of the AAO graded-lattice PCH at different chemicals with increasing refractive index taken by Sony QX-100 camera. Table 1 shows the calculated CIELab coordinates for the colorimetric response of our AAO graded-lattice PCH with five analytes, represented by the L*, a*, and b* listed in increasing refractive index order. The calculated points mapped from the images onto CIE 1931 chromaticity diagram is shown in Fig. 5(b).

We observe the color change affects all the tristimulus values with gradual decrease of the brightness L*. However, within small lightness change of ΔL* = 4 between points 2 and 3 or ΔL* = 2 between points 4 and 5, the difference of the quantitative differences ΔE are more than 1 with respect to 0.01 RIU change. Since ΔE between the two different images corresponds to the minimal distance between the two point in the Lab-coordinate system, there are at least ΔE number of perceptually recognizable color differences between the two different color images with respect to the refractive index unit. This result shows that refractive index difference down to ~ 0.01 can be distinguished by human perception with our AAO graded-lattice PCH sensor.

Table 1.

	Analytes	RI	L*	a*	b*	dE/d(0.01RIU)
1	Air	1	86	-40	-22	
2	Water	1.3323	78	-6	39	dE_{23} ~1.7956
3	2-propanol (IPA)	1.3740	74	-8	33	dE_{34}~3.3817
4	cyclohexane	1.4225	66	-5	19	dE_{45}~2.4439
5	trichloroethylene	1.4777	64	-2	6	

We note that it is also possible to increase the distance ΔE between different refractive indices in the CIELab space by increasing lightness condition differences ΔL*. Therefore, the color images taken under brighter illumination would be more effective for the perceptual refractive index sensing.

Conclusions

In conclusion, novel high Q-factor graded-lattice heterostructure of AAO PC is achieved by pulsed anodization and controlled etching process for highly sensitive refractive index sensor. FDTD simulations demonstrated that the resonant transmission, which is arose around the graded-lattice heterostructure, achieved distinct peaks with higher energy. By breaking periodicity symmetry, high Q-factor of ~ 55 can be obtained from the first order peaks at higher side energy band, which is almost twice higher value than previous reported results[12, 16]. Moreover, the first order peak in the reflection spectra has strong linear relationship with the refractive index. This relationship leads to sensitivity as high as $d\lambda/dn$ ~ 441 nm/RIU; four-fold enhanced sensitivity compared to the previous report[13]. Allowing efficient analyte infiltration into AAO PCH template, 3D interconnected nanochannel network enabled polarity-independent refractive index sensing. Colorimetric sensing ability is analyzed with CIELab color system, demonstrating that our sensor responds to small refractive index changes down to ~ 0.01RIU with a perceptual color change over a whole visible range. In this study, we have concentrated on optical properties of AAO PCH; however, their potential to provide excellent sensing platform with surface functionalization, which grants the opportunities to AAO PCH as a powerful candidates in various research fields, should also be focused.

Additional notes

Characterization methods

Cross section SEM micrographs were obtained in a Hitachi S4800 field emission microscope for samples fractured by external forces. The samples were sputtered with thin layer of Pt prior to imaging. A Vis-NIR spectrometer (Ocean Optics, USB2000+) was employed to detect the normal angle reflectance spectrum in the range of 400-900 nm with a fiber-coupled halogen light source (Ocean Optics, HL-2000). Color information was obtained using commercial software Photoshop CS6 (Adobe Systems Inc.). We followed similar method of application of Photoshop software to relative comparison of colors using high correlation of obtained tristimulus values between Photoshop and commercial colorimeter.[33] Detailed methodology including color analysis and converting images into CIE standard Lab color spaces can be found in the literature.[34]

Finite-Difference Time-Domain (FDTD) simulations

A commercial FDTD package (Lumerical Solutions Inc.) was used to calculate the optical responses of AAO graded-lattice PCH. The irradiation source was a normal-incidence plane wave propagating in the vertical direction. Periodic boundary conditions were imposed at the boundaries of the x-y plane assuming semi-infinite space along the horizontal direction. The optical properties of materials were taken from Palik's handbook.[35]

Acknowledgements

This research was supported by Basic Science Research Program and the Pioneer Research Center Program through the National Research Foundation of Korea (NRF) funded by the Ministry of Science, ICT and Future Planning (NRF-2015R1A2A2A11001112, NRF-2013M3C1A3065045) and the Low Observable Technology Research Center program of the Defense Acquisition Program Administration and Agency for Defense Development. The authors gratefully thank to Junhyun Kim and Yeon hong Kim for careful feedback and discussions.

References

1. G. Kang, J. Yoo, J. Ahn and K. Kim, *Nano Today*, 2015, **10**, 22-47.
2. J. D. Joannopoulos, S. G. Johnson, J. N. Winn and R. D. Meade, *Photonic Crystals: Molding the Flow of Light*, Princeton University Press, Princeton, NJ, 2008.
3. Z. Wang, J. Zhang, J. Xie, C. Li, Y. Li, S. Liang, Z. Tian, T. Wang, H. Zhang, H. Li, W. Xu and B. Yang, *Advanced Functional Materials*, 2010, **20**, 3784-3790.
4. M. M. Hawkeye and M. J. Brett, *Advanced Functional Materials*, 2011, **21**, 3652-3658.
5. C. Liu, G. Gao, Y. Zhang, L. Wang, J. Wang and Y. Song, *Macromolecular Rapid Communications*, 2012, **33**, 380-385.
6. L. Passoni, L. Criante, F. Fumagalli, F. Scotognella, G. Lanzani and F. Di Fonzo, *ACS Nano*, 2014, **8**, 12167-12174.
7. V. S.-Y. Lin, K. Motesharei, K.-P. S. Dancil, M. J. Sailor and M. R. Ghadiri, *Science*, 1997, **278**, 840-843.
8. D.-L. Guo, L.-X. Fan, F.-H. Wang, S.-Y. Huang and X.-W. Zou, *The Journal of Physical Chemistry C*, 2008, **112**, 17952-17956.
9. A. M. Ruminski, B. H. King, J. Salonen, J. L. Snyder and M. J. Sailor, *Advanced Functional Materials*, 2010, **20**, 2874-2883.
10. B. H. King, T. Wong and M. J. Sailor, *Langmuir*, 2011, **27**, 8576-8585.
11. M. M. Rahman, L. F. Marsal, J. Pallarès and J. Ferré-Borrull, *ACS applied materials & interfaces*, 2013, **5**, 13375-13381.
12. P. Yan, G. T. Fei, G. L. Shang, B. Wu and L. De Zhang, *Journal of Materials Chemistry C*, 2013, **1**, 1659-1664.
13. J. Ferré-Borrull, M. Rahman, J. Pallarès and L. Marsal, *Nanoscale Res Lett*, 2014, **9**, 1-6.
14. T. Kumeria, M. M. Rahman, A. Santos, J. Ferré-Borrull, L. F. Marsal and D. Losic, *ACS Applied Materials & Interfaces*, 2014, **6**, 12971-12978.
15. T. Kumeria, M. M. Rahman, A. Santos, J. Ferré-Borrull, L. F. Marsal and D. Losic, *Analytical Chemistry*, 2014, **86**, 1837-1844.
16. Y. Wang, Y. Chen, T. Kumeria, F. Ding, A. Evdokiou, D. Losic and A. Santos, *ACS Applied Materials & Interfaces*, 2015, **7**, 9879-9888.
17. Y. Y. Li, F. Cunin, J. R. Link, T. Gao, R. E. Betts, S. H. Reiver, V. Chin, S. N. Bhatia and M. J. Sailor, *Science*, 2003, **299**, 2045-2047.
18. A. Santos, V. S. Balderrama, M. Alba, P. Formentín, J. Ferré-Borrull, J. Pallarès and L. F. Marsal, *Advanced Materials*, 2012, **24**, 1050-1054.
19. M. Müller, R. Zentel, T. Maka, S. G. Romanov and C. M. Sotomayor Torres, *Advanced Materials*, 2000, **12**, 1499-1503.
20. Y. Su, G. T. Fei, Y. Zhang, H. Li, P. Yan, G. L. Shang and L. De Zhang, *J. Opt. Soc. Am. B*, 2011, **28**, 2931-2933.
21. B.-S. Song, S. Noda, T. Asano and Y. Akahane, *Nat Mater*, 2005, **4**, 207-210.
22. V. Agarwal and E. M.-R. Miguel, *Journal of Physics D: Applied Physics*, 2007, **40**, 3203.
23. W. Lee and S.-J. Park, *Chemical Reviews*, 2014, **114**, 7487-7556.
24. W. Lee, K. Schwirn, M. Steinhart, E. Pippel, R. Scholz and U. Gosele, *Nat Nano*, 2008, **3**, 234-239.
25. J. Martín, M. Martín-González, J. Francisco Fernández and O. Caballero-Calero, *Nat Commun*, 2014, **5**.
26. H. Masuda and K. Fukuda, *Science*, 1995, **268**, 1466-1468.
27. G. Meng, Y. J. Jung, A. Cao, R. Vajtai and P. M. Ajayan, *Proc. Natl. Acad. Sci. U. S. A.*, 2005, **102**, 7074-7078.
28. G. Kang, H. Park, D. Shin, S. Baek, M. Choi, D.-H. Yu, K. Kim and W. J. Padilla, *Advanced Materials*, 2013, **25**, 2617-2623.
29. H. Park, D. Shin, G. Kang, S. Baek, K. Kim and W. J. Padilla, *Advanced Materials*, 2011, **23**, 5796-5800.
30. I. De Graeve, H. Terryn and G. E. Thompson, *Journal of The Electrochemical Society*, 2003, **150**, B158-B165.
31. Y. Yin, H.-J. Schneider and M. Shahinpoor, *Responsive photonic nanostructures: Smart nanoscale optical materials*, Royal Society of Chemistry2013.
32. J. Schanda, *Colorimetry: Understanding the CIE System*, Wiley-Blackwell2007.
33. H. Afshari-Jouybari and A. Farahnaky, *Journal of Food Engineering*, 2011, **106**, 170-175.
34. *Adobe Photoshop CS6 User Guide*, Adobe Systems Inc2013.
35. E. D. Palik, *Handbook of Optical Constants of Solids*, Academic Press, Orlando, FL, 1997.